Accepted Manuscript

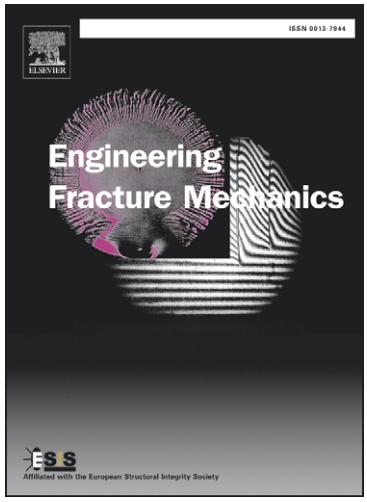

Cohesive Zone Modeling of Ductile Tearing Process in Brazed Joints

Morvarid K. Ghovanlou, Hamid Jahed, Amir Khajepour

PII: S0013-7944(12)00457-2
DOI: http://dx.doi.org/10.1016/j.engfracmech.2012.11.018
Reference: EFM 3926

To appear in: *Engineering Fracture Mechanics*

Received Date: 18 November 2011
Revised Date: 19 November 2012
Accepted Date: 24 November 2012

Please cite this article as: Ghovanlou, M.K., Jahed, H., Khajepour, A., Cohesive Zone Modeling of Ductile Tearing Process in Brazed Joints, *Engineering Fracture Mechanics* (2012), doi: http://dx.doi.org/10.1016/j.engfracmech.2012.11.018

Cohesive Zone Modeling of Ductile Tearing Process in Brazed Joints

Authors: Morvarid K. Ghovanlou[1]
Hamid Jahed[2]
Amir Khajepour[3]

1. Corresponding Author, Dept. of Mechanical and Mechatronics Engineering, University of Waterloo, 200 University Avenue West, Waterloo, Ontario, N2L 3G1, Canada
Email: mkarimig@uwaterloo.ca
Tel. +1 519 888-4567 ext. 37555
Fax. +1 519 885-58623

2. Professor, Dept. of Mechanical and Mechatronics Engineering, University of Waterloo, 200 University Avenue West, Waterloo, Ontario, N2L 3G1, Canada
Email: hjahed@uwaterloo.ca

3. Professor, Dept. of Mechanical and Mechatronics Engineering, University of Waterloo, 200 University Avenue West, Waterloo, Ontario, N2L 3G1, Canada
Email: a.khajepour@uwaterloo.ca

Abstract

Ductile tearing process in low carbon steel brazed joints with copper filler metal is studied using the Cohesive Zone Model. The Cohesive Zone Model is characterized by two parameters related to the cohesive strength and cohesive energy. A new method is developed to estimate the Cohesive Zone Model parameters through direct experimental measurements and numerical modeling. The cohesive energy of the brazed joints is obtained from the fracture test results performed on the single-edge notched bend specimens. Based on the obtained cohesive energy parameter, the fracture test is simulated using a cohesive zone finite element model. A unique value for the joint cohesive strength is determined by best fitting the finite element results to the experimental load-crack mouth opening displacement curves. The merit of the characterized Cohesive Zone Model is explored by finite element modeling of the tensile test performed on the

single-edge notched tension specimens. The load-crack mouth opening displacement curve obtained from the finite element modeling conforms to the corresponding tensile test results. Furthermore, the effect of the crack tip stress constraint on the plastic zone shape and size is successfully captured by the model. The good agreement between the finite element simulation results and the experimental data demonstrates the applicability of the Cohesive Zone Model for fracture analysis of the brazed joints.

Keywords: cohesive zone modeling; brazed joint; ductile tearing; parameter characterization

Nomenclature

a	Crack length
A_{Vpl}	Plastic component of the area under load- crack mouth opening displacement curve
b	Ligament length
B	Fracture specimen thickness
D	Damage variable
E	Young's modulus
h	Constraint parameter
J_c	Critical energy release rate
J_{el}	Elastic component of the energy release rate
J_C^{el}	Elastic component of the critical energy release rate
J_{pl}	Plastic component of the energy release rate
J_C^{pl}	Plastic component of the critical energy release rate
k	Cohesive zone stiffness
K	Stress intensity factor
$L_{e,C}$	Continuum element length
$L_{e,CZM}$	Cohesive element length
P	Load
P_c	Critical load
P_{max}	Maximum load
S_{inner}	Inner loading span

S_{outer}	Outer loading span
t	Brazed joint clearance
W	Fracture specimen width
δ	Separation
δ_0	Separation at onset of damage initiation
δ_C	Separation at failure
Γ	Cohesive energy
σ_H	Hydrostatic part of stress
$\sigma_{max,0}$	Cohesive strength
σ_{Mises}	Equivalent Mises stress

1. Introduction

Brazing as a type of joining is widely used in industries to join separate parts of a structure. A filler metal in the form of foil, plating, paste, or wire with melting temperature of above 450°C and below the solidus point of the base metal is melted and diffused into the faying surfaces to form joint upon solidification [1].

The reliability of brazed joints against propagation of pre-existing defects and cracks relies on the joint ductility. Extensive experimental investigations have been carried out to evaluate the brazed joint ductility influenced by different brazing conditions [2–7]. Based on the conventional fracture mechanics theory, many researchers have used the fracture toughness parameter as the joint fracture criterion [8–13]. Interfacial stress intensity factors for fracture specimens have been calculated by the Finite Element (FE) modeling to estimate the joint toughness from fracture test results [9,12]. Moreover, the effect of brazing residual stresses on the joint fracture toughness has been studied by the FE method [9]. Although the brazed joint failure has been assessed based on the fracture toughness parameter in many investigations, it has been commonly accepted that the single-parameter fracture criterion shows dependency on the specimen geometry and loading configurations [2, 9, 14]. To the author's knowledge, a fracture analysis method capable of

predicting fracture, independent of geometry and loading has not yet been applied to the brazed joints.

The Cohesive Zone Model (CZM), as a two-parameter fracture analysis tool, is capable of interface fracture analysis, independent of geometry and loading. In the CZM approach the interfacial constitutive model is defined by a relation between traction and separation at the fracture process zone to model crack initiation and propagation [15]. The CZM is characterized by two parameters related to the cohesive strength and cohesive energy. The cohesive strength is the maximum traction attained within the fracture process zone at the onset of damage initiation, and the cohesive energy is the work needed for full material separation per unit area of the crack extension [16]. The CZM constitutive relation is such that, upon increasing the separation, the traction increases up to the limiting value of the cohesive strength; thereafter, traction gradually decreases and eventually vanishes at the onset of complete material separation [15]. Applicability of the CZM to fracture analysis of structures with material and geometrical nonlinearities is an important advantage of this approach [17]. Furthermore, this method is particularly capable of crack growth analysis at interfaces with complex crack tip fields [18]. Using the CZM, the energy needed for decohesion is decoupled from other dissipative mechanisms near the crack tip. This implies that the CZM characterized for an interface is capable of including the experimentally observed geometry and load dependencies of the interfacial crack growth behavior [18]. In many researches the CZM approach has been employed to simulate the decohesion phenomenon at the interface of adhesively bonded structures associated with considerable plastic deformation of adherents [19–21]. In addition, the CZM has achieved popularity in simulating fracture process in laminated [22–24], fiber [25–28], and honeycomb [29] composite material structures. The application of the CZM coupled to a cyclic damage evolution law has also been of interests for facture analysis of solder joints under cyclic loading condition [16, 30].

Merit of the CZM in different failure situations depends on the use of the proper model parameters in the analysis. In general, the cohesive strength and cohesive energy are characterized through experimental measurements associated with the FE simulations [21, 25, 31–35]. The two model parameters are often determined simultaneously by optimization techniques to minimize the difference between the simulation results and the experimental data

[31, 35]; however, the uniqueness of the obtained parameters is debatable [28]. On the other hand, a few researches have been conducted to directly measure one of the CZM parameters through experimental methods. Chandra [25] applied the CZM to study the interfacial failure in metal matrix composites. In this research, the interfacial work of separation was determined through quantifying the area under load-displacement curve obtained from a push-out test. Then using finite element simulation, the cohesive strength was adjusted such that the numerical results best fits the experimental data. Chen et al. [33] estimated the cohesive energy by topographic measurement of the corresponding fracture surface of the tensile specimens. Thereafter, the cohesive strength was determined by fitting the numerical crack length-load line displacement curve to the experimental results. Investigations have shown that characterization of one model parameter through direct experimental measurement and the other parameter through fitting the cohesive zone FE modeling results to the experimental data leads to a unique set of the model parameters [25, 33].

In this paper, a new method is developed to estimate the CZM parameters in a ductile tearing process through direct experimental measurements and numerical modeling. The cohesive energy is determined through decomposition of the critical energy release rate into the large scale plastic dissipations around the crack tip and the energy needed for material debonding within the fracture process zone. The application of the CZM has also been extended in this study to estimate the fracture strength and model the ductile tearing process in brazed joints. In the outlined method, the critical energy release rate, which includes large-scale plastic dissipations around the crack tip, is calculated from the results of the fracture test performed on the Single-Edge Notched Bend (SENB) specimens [2]. The elastic component of the critical energy release rate, which is the energy needed for debonding per unit area of the crack advance, is taken as the brazed joint cohesive energy. Based on the experimentally obtained cohesive energy, the fracture test is modeled by finite element using commercial software ABAQUS [36], and a unique value for the cohesive strength is determined by best fit to the experimental load-Crack Mouth Opening Displacement (CMOD) curves. Merit of the characterized cohesive zone FE model is examined by comparing the FE simulation results of the tensile test performed on the Single-Edge Notched Tension (SENT) specimens with the corresponding experimental data. The good agreement between the estimated and experimental results suggests the CZM parameter transferability to different geometry and loading configurations.

2. Experimental evaluation of the cohesive energy

2.1. Material and Experiment

Single edge notched brazed specimens with a starter crack ($a/W = 0.5$) were prepared for the fracture toughness testing. Blocks of low carbon steel (ASTM-A36), as the base metal, were furnace brazed using copper filler metal foil (BCu-1) at the temperature of 1110°C [2]. Four-point bending quasi-static fracture tests were performed on the SENB specimens. The schematic of the specimen with a thickness of $B = 7\ mm$ and its loading configuration is shown in Fig.1. The test was conducted under displacement controlled condition at a rate of 0.03 mm/s using a servo hydraulic tensile machine. Load and CMOD were recorded and the crack length was monitored by a Charge Coupled Device (CCD) video-microscope camera during the fracture test. Experimental results have shown that the crack propagates through the joint filler metal region, and no delamination occurs at the steel/copper interface [2]. Details of the experimental procedure for the specimen preparation and the fracture test are described in the reference [2].

Fig.1. Schematic of the SENB specimen with initial crack length *a* (dimensions in mm)

2.2. Experimental results

The load-CMOD curve along with the corresponding crack extension, provided in the reference [2], was used to evaluate the cohesive energy. The starter crack introduced inside the joint propagates when the energy release rate reaches its critical value. The experimental results indicate a stable tearing process through the copper filler metal region followed by instability at the final stage of the crack propagation. As is discussed in the reference [2], the predominant dimple rupture mechanism on the joint fracture surface, which was initiated at the dendrites and microvoids, implies the ductile tearing process. This tearing process is accompanied by the base metal plastic deformation around the crack tip, as is shown in Fig.2.

Fig.2. Optical micrograph of the SENB specimen at the crack tip region (a) 50x, (b) 100x showing the ductile tearing process within the copper filler metal and deformation in the base metal

The cohesive energy consists of the material surface energy and its accompanying small-scale inelastic dissipations at the immediate vicinity of the crack tip for the unit area of the surface created. Based on this concept, the critical energy release rate or the fracture energy is considered as the cohesive energy in brittle fracture [25, 37]. However, in ductile fracture the energy release rate also includes large-scale plastic dissipations around the crack tip region. Decomposition of the energy release rate into the elastic, J^{el}, and plastic, J^{pl}, components decouples the work required for material separation from the energy dissipation due to large-scale plasticity around the crack tip region [25, 37–40]. The elastic component of the critical energy release rate, J_C^{el}, which is the energy needed for material debonding per unit area of the crack advance, is considered as the cohesive energy of a ductile material [37]. As a result, the cohesive energy of the brazed joint consists of the brazing filler material surface energy and its corresponding inelastic deformations due to material separation within the brazed joint. The large scale plastic work of the base metal is not included in the cohesive energy; rather, it has been considered as the plastic component of the energy release rate and its amount increases as the crack propagates.

The elastic and plastic components of the J integral for each increment of the crack extension (i) are calculated from the load, CMOD, and crack length measured from the fracture test, as follows:

$$J = J_{el} + J_{pl} \tag{1}$$

$$J_{el(i+1)} = \frac{K_{(i+1)}^2}{\acute{E}} \tag{2}$$

$$J_{pl(i+1)} = \left(J_{pl(i)} + \frac{\eta_{CMOD}^i}{b_i B} A_{Vpl}^{i+1,i}\right)\left(1 - \frac{\gamma_{CMOD}^i}{b_i}(a_{i+1} - a_i)\right) \tag{3}$$

where $\acute{E} = E$ for plane stress and $\acute{E} = E/(1-\nu^2)$ for plane strain conditions [37].

The stress intensity factor, $K_{(i+1)}$, is defined as:

$$K_{(i+1)} = \frac{P_{(i+1)}}{BW^{\frac{1}{2}}} f\left(\frac{a_{(i+1)}}{W}\right) \tag{4}$$

where W and B are the specimen width and thickness, respectively. In the above equations, two subsequent increments of the crack extension have been identified by the indices of (i) and (i+1). Furthermore, a is the crack length and $f\left(\frac{a}{w}\right)$ is a dimensionless weight function which is defined by Eq. (5) for the SENB specimen [37]:

$$f\left(\frac{a}{w}\right)=\frac{3\frac{(S_{outer}-S_{inner})}{W}(\frac{a}{W})^{1/2}\left[1.99-\left(\frac{a}{W}\right)\left(1-\frac{a}{W}\right)\left(2.15-3.93\left(\frac{a}{W}\right)+2.7\left(\frac{a}{W}\right)^{2}\right)\right]}{2\left(1+2\frac{a}{W}\right)\left(1-\frac{a}{W}\right)^{3/2}} \quad (5)$$

where S_{outer} and S_{inner} are the outer and inner loading spans shown in Fig.1, respectively [37].

In Eq. (3), the increment of the plastic component of the area under load-CMOD curve is indicated by $A_{\mathrm{V}pl}^{i+1,i}$. Further, for the SENB specimens, the geometry factors of γ_{CMOD} and $\eta_{CMOD}=3.667-2.199\left(\frac{a_0}{W}\right)+0.437\left(\frac{a_0}{W}\right)^{2}$ are given equal to 0.9 and 2.68, respectively [41].

Using Eq.s (1) through (5), the elastic and plastic components of the critical energy release rate are calculated from the experimentally measured load, CMOD, and crack length of the fracture test provided in reference [2]. The obtained value of the critical energy release rate at the onset of physical crack extension, excluding the crack extension due to blunting, is provided in Table 1. The plastic component of the energy release rate corresponds to the base metal plastic work dissipated around the crack tip, whereas the elastic part of the critical energy release rate represents the brazed joint cohesive energy.

Table 1. Components of critical energy release rate of the SENB specimen

Specimen	$\boldsymbol{J_C^{el}}$ $[\frac{\boldsymbol{kJ}}{\boldsymbol{m^2}}]$	$\boldsymbol{J_C^{pl}}$ $[\frac{\boldsymbol{kJ}}{\boldsymbol{m^2}}]$	$\boldsymbol{J_C}$ $[\frac{\boldsymbol{kJ}}{\boldsymbol{m^2}}]$
SENB	6.3	60.4	66.7

The fracture test results indicate that the plane stress condition is dominant in the fracture process of the SENB specimens. According to Eq. (6), if the values of the specimen thickness, B, and the initial crack ligament, b_0, are less than the experimentally obtained value of $25J_c/\sigma_Y$, the plane stress condition is dominant in the fracture test. Otherwise, the fracture test is assumed to be conducted under the plane strain condition [33,37,42].

$$B, b_0 < \frac{25J_c}{\sigma_Y} \tag{6}$$

Substituting the values of the critical energy release rate and the base metal yield strength into Eq. (6) gives:

$$B, b_0 < \frac{25J_c}{\sigma_Y} = \frac{25 \times 66.7 \left[\frac{kJ}{m^2}\right]}{219\ [MPa]} = 7.6\ [mm]$$

Since B and b_0 are equal to 7 mm, the above inequality is valid for the tested specimens and the plane stress condition is a suitable assumption to model the fracture process in this study.

3. Evaluation of the cohesive strength through FE simulation

3.1. FE modeling of the bending test

Ductile tearing process of the SENB brazed specimens under the four-point bend quasi-static fracture test is modeled using ABAQUS [36]. The built-in cohesive elements (COH2D4) with 4 nodes and 2 integration points are used in the simulation. The brazed joint interlayer is meshed by a single row of the two-dimensional cohesive elements oriented in the joint thickness direction. The initial constitutive thickness of the cohesive elements is set equal to the joint clearance of 0.05 mm. A bilinear traction-separation law, shown in Fig. 3, is used as the constitutive model of such cohesive elements. The relation between the CZM parameters related to the cohesive energy, Γ, and the cohesive strength, $\sigma_{max,0}$, is given by Eq. (7):

$$\Gamma = \frac{1}{2}\sigma_{max,0}\delta_C \tag{7}$$

where δ_C represents the separation at failure [25].

The cohesive energy obtained from the experiment is assigned to the cohesive elements. The cohesive zone stiffness which is equal to the slope of the linear elastic part of the traction-separation law is defined by [36]:

$$k = \frac{E}{t} \tag{8}$$

where E and t represent Young's modulus of the joint copper filler metal, i.e., 82 GPa, and the joint clearance, i.e., 0.05 mm, respectively [2].

Fig.3. Bilinear traction-separation law used in the FE simulation

The surrounding base metal regions are meshed by 4-node quadrilateral bilinear elements (CPS4R) [36]. Elastic properties of the base metal are Young's modulus of 200 GPa and Poisson's ratio of 0.3. The hardening behavior of the base metal is taken from the tensile tests and the corresponding stress values versus the plastic strains are provided in Table 2 [2].

Table 2. The stress values versus the plastic strains for the base metal

Plastic strain [mm/mm]	0	0.014	0.030	0.040	0.050	0.060	0.070	0.100
Stress [MPa]	219	220	270	290	308	322	332	360

The FE model of the SENB specimen and its boundary conditions are shown in Fig. 4 (a). Fixed displacement boundary conditions are applied to the top rigid rollers, and the bottom rigid rollers are displaced upward. Surface to surface contact is used between the rollers and specimen with a refined mesh at the contact regions. The CMOD is obtained from the x-displacement of the knife edges which have been included in the FE model. The mesh patterns around the crack path and at the tip of the crack are illustrated in Figs. 4 (b) and (c), respectively.

Fig.4. (a) FE model of the SENB specimens and boundary conditions, (b) mesh pattern around the crack path, (c) mesh pattern at the crack tip

A mesh convergence study is carried out to obtain a proper cohesive element length, $L_{e,CZM}$. The initial cohesive element length of 0.02 mm is selected first and the number of elements is doubled in the subsequent mesh convergence analysis. The obtained numerical CMOD-crack extension curves for different cohesive element lengths are plotted in Fig.5. The numerical results are convergent for the cohesive element length of 0.005 mm which is used in the FE simulations and is shown in Fig 4(c).

Fig.5. CMOD-crack extension curves for different cohesive element mesh sizes $L_{e,CZM}$ measured in mm

In order to capture the plastic deformation around the crack tip, the surrounding continuum elements should be sufficiently fine. An initial element length, $L_{e,C}$, of 0.12 mm is selected for such elements, and the number of elements is doubled in the subsequent FE analysis. The load-CMOD curves for different mesh sizes are presented in Fig. 6. The FE results are convergent for $L_{e,C}$=0.02 mm which is the size used in the FE simulations. The calculated cohesive energy of 6.3 kJ/m^2 and a cohesive strength of 400 MPa were used as the CZM parameters in the mesh convergence study with the plane stress assumption.

Fig.6. Load-CMOD curves for different continuum element mesh sizes $L_{e,c}$ measured in mm

3.2. FE modeling results

Figure 7 shows the numerical load-CMOD curves obtained for a range of cohesive strength values to match the corresponding experimental results. It can be observed that the FE results with the cohesive strength of 395±2 MPa best fit the experimental curves. The critical load, P_C , and the maximum load, P_{max}, are obtained to be equal to 2.08 kN and 2.13 kN for the cohesive strength of 395 MPa, respectively.

Fig.7. Numerical load-CMOD curves with different values of $\sigma_{max,0}$ fitted to the experimental results

The obtained critical and maximum loads with respect to the cohesive strength values with a variation of ±2 MPa are plotted in Fig. 8. The results show that the maximum attainable load is more sensitive than the critical load with respect to the variations of the cohesive strength.

Fig. 8. Variations of the critical and maximum loads with respect to the cohesive strength

Using the obtained cohesive strength, the FE modeling is performed to assess the sensitivity of the predicted results to any error in the cohesive energy calculations. Values of the critical and maximum loads with respect to the error percentage of about ±15% corresponding to the cohesive energy of 6.3±1 kJ/m^2 are presented in Fig. 9. The results of the sensitivity analysis show that the critical and maximum loads have a variation of 1% and 2% to ±15% variation of the cohesive energy, respectively.

Fig.9. Variations of the critical and maximum loads with respect to the cohesive energy

Figure 10 shows the contour plots of the stress perpendicular to the crack faces at different stages of crack initiation and propagation. The corresponding numerical values of the traction distribution along the interlayer are plotted in Fig. 11. Before damage initiation in each cohesive element, increasing the separation leads to continuous increase of the traction (Fig.10 (b)). The damage initiates once the traction reaches the cohesive strength of 395 MPa in each cohesive element. The onset of damage initiation in the first cohesive element located at the initial crack tip is shown in Fig.10 (c). Further increase in the separation results in the gradual degradation of the damage-initiated cohesive elements along the interlayer. Accordingly, the traction drops below the cohesive strength of 395 MPa and reaches zero for the first fully damaged cohesive element to simulate crack initiation (Fig.10 (d)). Afterwards, the elements which are fully damaged are subsequently removed to simulate crack propagation (Fig.10 (e)). The gradual degradation of the cohesive elements, which leads to the gradual loss of element's load carrying capacity, makes the CZM approach suitable to simulate ductile tearing process through the brazed joint interlayer.

Fig.10. Stress, S22, perpendicular to crack faces (a) in the whole model at crack initiation, (b) before damage initiation, (c) at the onset of damage initiation, (d) at the onset of crack initiation, (e) during crack propagation

Fig.11. Traction distributions from the initial crack tip along interlayer at different damage levels

The reliability of the characterized CZM is further evaluated through the value of the energy release rate. Based on the finite element results and using the analytical relation given in Eq.s (1) through (5), the energy release rate is calculated for the subsequent steps of the crack extension. It is assumed that the crack growth steps are equal to the length of the damage band created due to formation and growth of micro-voids ahead of the crack tip [43]. Using the finite element results, the damage variable for the bilinear CZM characterized in this study is calculated from Eq. (9) and plotted in Figs. 12 and 13 [36]:

$$D = \frac{\delta_C(\delta - \delta_0)}{\delta(\delta_C - \delta_0)} \tag{9}$$

where $\delta \geq \delta_0,\ \delta_0 = \sigma_{max,0}/k = 0.0002\ mm$ and $\delta_C = 2\Gamma/\sigma_{max,0} = 0.0319\ mm$.

As shown in Fig. 13, the length of the damage band at the onset of crack initiation ($\Delta a = 0$) is obtained equal to 0.25 mm, which is the length of the next crack growth step. For the subsequent step of the crack extension ($\Delta a = 0.25\ mm$), the length of the damage band measured from the initial crack tip is obtained to be equal to 0.33 mm, as shown in Fig.13.

Fig. 12. Distribution of the damage variable (SDEG) along the interface (a) at the onset of crack initiation, (b) after one step crack extension ($\Delta a = 0.25\ mm$)

Fig. 13. Damage distribution from the initial crack tip along the interface

The energy release rate at the onset of crack initiation and for the two subsequent crack growth steps is calculated and provided in Table 3. The results show that the value of the J integral obtained from the cohesive zone FE modeling at the second crack growth step ($\Delta a = 0.33\ mm$) is in excellent agreement with the experimental value of J_C given in Table 1.

Table 3. Values of the J integral calculated from the FEM results for the subsequent crack extensions

$\Delta a\ [mm]$	0	0.25	0.33
$J(\Delta a)\ [\frac{kJ}{m^2}]$	23.7	44.8	66.9

4. CZM application and discussion

4.1. Experiment

In order to explore the applicability of the CZM to fracture estimation of the brazed joints, tensile tests were performed on the SENT specimens and simulated by the characterized cohesive zone FE model. Figure 14 shows the schematic of the SENT specimen with a starter crack ($a/W = 0.5$) under the applied loading. The tension tests were conducted by a servo-hydraulic tensile machine under a displacement controlled condition with a rate of 0.03 mm/s. The SENT specimens were tested with the clamping distance of 60 mm. Similar to the four-point bending test, load and CMOD were recorded, and the crack length was monitored by a CCD video-microscope camera.

Fig.14. SENT specimen under tensile loading (dimensions in mm) [2]

4.2. FE modeling of the tension test

The FE model of the SENT specimen and the corresponding boundary conditions are illustrated in Fig.15. One end of the model is fixed and displacement along the specimen axis is applied to the other end of the model. The two knife edges are also included in the model for CMOD measurements. The same element sizes obtained for the modeling of the SENB specimen are used in this simulation.

Fig.15. FE model of the SENT specimen and the applied boundary conditions

4.3. Results and discussion

The load-CMOD curve obtained from the FE simulation in the plane stress condition is plotted over the experimental curve (Fig.16). The results show that the ductile tearing process in the SENT specimen is well estimated by the characterized cohesive zone FE model.

Fig.16. Experimental and numerical load-CMOD curves of the SENT specimen

The critical load at crack initiation and the maximum attainable load obtained from the simulations and the experiments for the SENB and SENT specimens are presented and compared in Table 4. The numerical results are in a good agreement with the experimental data.

Table 4. The critical and maximum loads obtained from the CZM and experiment

Specimen type	CZM		Experiment	
	P_C [kN]	P_{max} [kN]	P_C [kN]	P_{max} [kN]
SENB	2.08	2.13	1.85	2.11
SENT	11.15	11.32	11.01	11.81

Contours of the crack tip plastic strain in the SENB and SENT specimens at the onset of crack initiation, during crack propagation, and at the onset of failure are plotted in Fig.17. Under the tensile loading, two slip shear bands are formed and developed at a ±55° angle with respect to the loading axis. In bending, the slip bands form a fan-shaped curvature known as Prandtl slip fields [40]. Furthermore, the crack tip plastic zones at failure, which are estimated by the cohesive zone FE model for the SENB and SENT specimens, are superposed on the optical micrographs taken from the specimen side surface near the crack after the fracture tests, as is shown in Fig. 18. The figure shows that, for both types of the specimens, the shape and size of the plastic zones obtained from the simulations are qualitatively in good agreement with the permanent deformations observed on the specimen micrographs.

Fig.17. Contours of crack tip plastic strain in the SENB specimen (a) at crack initiation, (b) during crack propagation, (c) at the onset of failure, and in the SENT specimen (d) at crack initiation, (e) during crack propagation, (f) at the onset of failure

Fig.18. FE estimated plastic zones (blue lines) at the onset of failure superposed on the optical micrographs of the adjacent crack path regions of the (a) SENT and (b) SENB specimens

The width of the plastic zone, obtained from the FE modeling, with respect to the crack extension for the two types of the fracture specimens is plotted in Fig. 19. In the SENB specimen

the size of the plastic zone gradually increases after crack initiation until a constant size is reached. However, in the SENT specimen the plastic zone size at the onset of crack initiation is larger than that of the SENB specimen, and a fast growing plastic zone is observed as the crack propagates until it reaches a flat plateau. As is shown in Fig. 19, for both types of the specimens the load increases during the development of the plastic zone and reaches its maximum value once the plastic zone size stabilizes. Thereafter, the total energy required for crack propagation, i.e., the summation of the plastic dissipation energy and the cohesive energy, remains constant. As a result, the external work of the applied displacement remains constant and the load drops to satisfy the energy balance.

Fig.19. Load and crack tip plastic zone width with respect to the crack extension

The crack tip plastic zone size depends on the stress state which is indicated by the stress constraint parameter (h). This parameter is defined as the ratio of the hydrostatic part of stress, σ_H, to the equivalent Mises stress [44, 45],

$$h = \frac{\sigma_H}{\sigma_{Mises}} \tag{10}$$

where

$\sigma_H = \frac{1}{3}\sigma_{ii}$, $i = 1,2,3$, and summation applies over the repeated indices

The high the parameter h, the more constraint on the plastic flow at the crack tip region. Figure 20 shows the crack tip constraint parameter plotted over the crack extension. For both types of the specimens, the crack tip constraint parameter increases during initial stages of the crack extension, reaches a maximum value and thereafter gradually decreases as the crack propagates. The stress constraint parameter for the SENT specimen has lower values than that of the SENB specimen, and decreases faster due to the crack extension. This implies that the plastic flow at the crack tip of the SENT specimen is less constrained, and the corresponding plastic zone more develops than that of the SENB specimen (Fig 19) [46]. Therefore, the effect of the crack tip stress constraint on the plastic zone shape and size seems to be well captured by the model. The good agreement observed between the results of the tension test simulation and the experiment

suggests that the characterized CZM for fracture estimation of the brazed joints is independent of geometry and loading configurations.

Fig.20. Crack tip constraint parameter with respect to crack extension for the SENB and SENT specimens

5. Conclusions

In this study the bilinear CZM, as a two-parameter fracture analysis tool, has been successfully employed to estimate Mode-I fracture and simulate the ductile tearing process in the low carbon steel brazed joints with copper filler metal. Using the CZM, the energy needed for material debonding is decoupled from the large scale plastic work dissipated around the crack tip. Hence, the characterized CZM is capable of modeling nonlinear fracture behavior of the brazed joints, independent of geometry and loading configurations. The CZM parameters related to the cohesive strength and the cohesive energy have been characterized from the four-point bend fracture test results and the corresponding FE simulation. The merit of the obtained CZM is investigated by the FE modeling of the tensile test performed on the SENT specimens. The following conclusions are drawn from this study:

1. The experimental observations indicate a stable tearing process through the copper filler metal region followed by instability at the final stage of the crack propagation. The predominant dimple rupture mechanism observed on the joint fracture surface implies the ductile tearing process. The low carbon steel base metal parts experience large scale plastic deformation around the crack tip as the crack propagates.
2. The cohesive energy, as one of the CZM parameter, is directly obtained from the fracture test results on the pre-cracked SENB specimens. Excluding the base metal plastic work dissipated around the crack tip, the elastic component of the critical energy release rate, i.e., the energy needed for material separation per unit area of the crack advance, is the joint cohesive energy in the ductile tearing process, and has been found to be equal to 6.3 kJ/m^2 for the steel/Cu/steel brazed joints. However, if the base material remains elastic or the crack tip plastic zone is in the range of small scale yielding, the entire critical energy release rate can be considered as the cohesive energy of a brazed joint.

3. The cohesive strength, as the second CZM parameter, is determined through relating the finite element modeling results to the experimental load-CMOD curves of the fracture test performed on the SENB specimens. The FE results with the cohesive strength of 395±2 MPa best fit the experimental curves.
4. To examine the applicability of the characterized CZM for the steel/Cu/steel brazed joints, the tensile test performed on the SENT specimens has been modeled. The obtained load-CMOD curve from the FE model is in good agreement with the corresponding experimental results. The agreement between the FE simulation results and the experimental data shows the uniqueness of the obtained CZM parameters. This indicates that, once the CZM parameters are determined for a brazed joint, the CZM is capable of estimating the joint fracture, independent of geometry and loading configurations.
5. Superposition of the plastic zone obtained from the FE simulation on the micrographs of the fracture specimens reveals that the shape and size of the plastic zone for both types of the specimens are well estimated by the cohesive zone approach. This indicates that effect of the crack tip stress constraint on the plastic zone is well captured by the model. The low crack tip constraint parameter in the SENT specimens results in a more developed plastic zone than that of the SENB specimens. Furthermore, the simulation results show that, for both types of the specimens, the load increases during the development of the plastic zone and reaches its maximum value once the plastic zone size stabilizes. Afterwards the total energy required for crack propagation remains constant, and the load drops to satisfy the energy balance.

Acknowledgment

The financial support of the Natural Sciences and Engineering Research Council of Canada, NSERC Strategic Grant Program, is acknowledged.

References

[1] Messler RW. Joining of Materials and Structures. USA: Elsevier; 2004.

[2] Ghovanlou MK, Jahed H, Khajepour A. Mechanical reliability characterization of low carbon steel brazed joints with copper filler metal. Mater Sci Eng A 2011; 528:6146–6156.

[3] Yu YH, Lai MO. Effects of gap filler and brazing temperature on fracture and fatigue of wide-gap brazed joints. J Mater Sci 1995; 30:2101–2107.

[4] Chen S, Chin BA. Low activation braze joint of dispersion-strengthened copper. J Nuclear Mater 1995; 225:132–136.

[5] Feng JC, Liu D, Zhang LX, Lin XC, He P. Effects of processing parameters on microstructure and mechanical behavior of SiO2/Ti–6Al–4V joint brazed with AgCu/Ni interlayer. Mater Sci Eng A 2010; 527:1522–1528.

[6] Nishi H, Kikuchi K. Influence of Brazing Conditions on the Strength of Brazed Joints of Alumina Dispersion-Strengthened Copper to 316 Stainless Steel. J Nuclear Mater 1998; 258–263:281–288.

[7] Gao F, Qiana Y. Micromechanical properties of heterogeneous aluminum-silicon brazed joint. Mater Lett 2004; 58:2861–2866.

[8] Moorhead AJ, Becher PF. Adaptation of the DCB test for determining fracture toughness of brazed joints in ceramic materials. J Mater Sci 1987; 22:3297–3303.

[9] Fu L, Miyasita Y, Mutoh Y. Fracture Toughness of Si3N4/S45C Joint with an Interface Crack. J Mater Online 2005; 1.

[10] Kobayashi H, Arai Y, Nakamura H, Sato T. Strength Evaluation of Ceramic-Metal Joints. Mater Sci Eng A 1991; 143:91–102.

[11] Leinenbach C, Schindler HJ, Baser TA, Rüttimann N, Wegener K. Quasistatic fracture behaviour and defect assessment of brazed soft martensitic stainless steel joints. Eng Fail Anal 2010; 17:672–682.

[12] Philips NR, He MY, Evans AG. A wedge fracture toughness test for intermediate toughness materials: Application to brazed joints. Acta Mater 2008; 56:4593–4600.

[13] Gan YX, Aglan HA, Steward RV, Chin BA, Grossbeck ML. Microstructure-fracture toughness relationship of vanadium alloy/stainless steel brazed joints. J Nuclear Mater 2001; 299:157–164.

[14] Nyhus B, Polanco ML, Orjasater O. SENT Specimens an Alternative to SENB Specimens for Fracture Mechanics Testing of Pipelines, Proceedings of 22nd International Conference on Offshore Mechanics and Arctic Engineering, Cancun, Mexico, 2003.

[15] Needleman A. A continuum model for void nucleation by inclusion debonding. J Appl Mech 1987; 54:525–531.

[16] Yang QD, Shim DJ, Spearing SM. A cohesive zone model for low cycle fatigue life prediction of solder joints. Microelec Eng 2004; 75:85–95.

[17] Chaboche JL, Feyel F, Monerie Y. Interface debonding models: a viscous regularization with a limited rate dependency. Int J Solids Struct 2001; 38:3127–3160.

[18] Roe KL, Siegmund T. An irreversible cohesive zone model for interface fatigue crack growth simulation. Eng Frac Mech 2003; 70:209–232.

[19] Tvergaard V, Hutchinson JW. On the toughness of ductile adhesive joints. J Mech Phys Solids 1996; 44:789–800.

[20] Tvergaard V, Hutchinson JW. Toughness of an interface along a thin ductile layer joining elastic solids. Philos Mag A 1994; 70:641–656.

[21] Yang QD, Thouless MD, Ward SM. "Elastic-plastic mode II of adhesive joints, Int J Solids Struct 2001; 38:3251–3262.

[22] Zou Z, Reid SR, Li S. A continuum damage model for delaminations in laminated composites. J Mech Phys Solid 2003; 51:333–356.

[23] Yang Q, Cox B. Cohesive models for damage evolution in laminated composites. Int J Fract 2005; 133:107–137.

[24] Meo M, Thieulot E. Delamination modeling in a double cantilever beam. Compos Struct 2005; 71:429–434.

[25] Chandra N, Li H, Shet C, Ghonem H. Some issues in the application of cohesive zone models for metal–ceramic interfaces. Int J Solids Struct 2002; 39:2827–2855.

[26] Fan C, Ben Jar PY, Cheng JJR. Cohesive zone with continuum damage properties for simulation of delamination development in fiber composites and failure of adhesive joints. Eng Frac Mech 2008; 75:3866–3880.

[27] Xie D, Salvi AG, Sun C, Waas AM. "Discrete Cohesive Zone Model to Simulate Static Fracture in 2D Triaxially Braided Carbon Fiber Composites. J Compos Mater 2006; 40: 2025–2046.

[28] Blackman BRK, Hadavinia H, Kinloch AJ, Williams JG. The use of a cohesive zone model to study the fracture of fiber composites and adhesively-bonded joints. Int J Fract 2003; 119:25–46.

[29] Han TS, Ural A, Chen CS, Zehnder AT, Ingraffea AR, Billington SL. Delamination buckling and propagation analysis of honeycomb panels using a cohesive element approach. Int J Fract 2002; 115:101–123.

[30] Abdul-Baqi A, Schreurs PJG, Geers MGD. Fatigue damage modeling in solder interconnects using a cohesive zone approach. Int J Solids Struct 2005; 42:927–942.

[31] Que NS, Tin–Loi F. Numerical evaluation of cohesive fracture parameters from a wedge splitting test. Eng Fract Mech 2002; 69:1269–1286.

[32] Sørensen B F, Jacobsen TK. Determination of cohesive laws by the J-integral approach. Eng Fract Mech 2003; 70:1841–1858.

[33] Chen CR, Kolednik O, Scheider I, Siegmund T. On the determination of the cohesive zone parameters for the modeling of micro-ductile crack growth in thick specimens. Int J Fract 2003; 120:517–536.

[34] Liljedahl CDM, Crocombe AD, Wahab MA, Ashcroft IA. Damage modeling of adhesively bonded joints. Int J Fract 2006; 141:147–161.

[35] Salomonsson K, Andersson T. Modeling and parameter calibration of an adhesive layer at the meso level. Mech Mater 2008; 40:48–65.

[36] ABAQUS/CAE, Version 6.7–1, Dassault Systems, 2007.

[37] Anderson TL. Fracture Mechanics: Fundamentals and Applications. 3rd ed. USA: Taylor and Francis; 2005.

[38] Jiang LM, Zhou YC, Liao YG, Sun CQ. A pressurized blister test model for the interface adhesion of dissimilar elastic–plastic materials. Mater Sci Eng A 2008; 487:228–234.

[39] Thouless MD, Adams JL, Kafkalidis MS, Ward SM, Dickie RA, Westerbeek GL. Determining the toughness of plastically deforming joints. J Mater Sci 1998; 33:189–197.

[40] Flores KM, Dauskardt RH. Enhanced Toughness Due to Stable Crack Tip Damage Zones in Bulk Metallic Glass. Scripta Mater 1999; 41:937.

[41] Standard Test Method for Measurement of Fracture Toughness, Designation: E 1820 – 08a, ASTM International, 2008.

[42] Gross D, Seelig T. Fracture Mechanics with an Introduction to Micromechanics. Netherlands: Springer; 2006.

[43] Wnuk MP, Bazant ZP, Law E. Stable growth of fracture in brittle aggregate materials. Theo Appl Fract Mech 1984; 2:259-286.

[44] Mirone G. Role of stress triaxiality in elastoplastic characterization and ductile failure prediction. Eng Fract Mech 2007; 74:1203–1221.

[45] Reuter WG, Underwood JH, Newman JC. Surface-Crack Growth: Models, Experiment, and Structures. Nevada: ASTM, STP1060; 1990.

[46] O'Dowd NP, Shih CF. Family of Crack Tip Fields Characterized by a Triaxiality Parameter-I. Structure of Fields. J Mech Phys Solids 1991; 39:989–1015.

Table 1. Components of critical energy release rate of the SENB specimen

Specimen	$J_C^{el}\ [\frac{kJ}{m^2}]$	$J_C^{pl}\ [\frac{kJ}{m^2}]$	$J_C\ [\frac{kJ}{m^2}]$
SENB	6.3	60.4	66.7

Table 2. The stress values versus the plastic strains for the base metal

Plastic strain [mm/mm]	0	0.014	0.030	0.040	0.050	0.060	0.070	0.100
Stress [MPa]	219	220	270	290	308	322	332	360

Table 3. Values of the J integral calculated from the FEM results for the subsequent crack extensions

$\Delta \boldsymbol{a}$ $[\boldsymbol{mm}]$	0	0.25	0.33
$\boldsymbol{J}(\Delta \boldsymbol{a})$ $[\frac{\boldsymbol{kJ}}{\boldsymbol{m^2}}]$	23.7	44.8	66.9

Table 4. The critical and maximum loads obtained from the CZM and experiment

Specimen type	CZM		Experiment	
	P_C [kN]	P_{max} [**kN**]	P_C [kN]	P_{max} [**kN**]
SENB	2.08	2.13	1.85	2.11
SENT	11.15	11.32	11.01	11.81

Figure 1

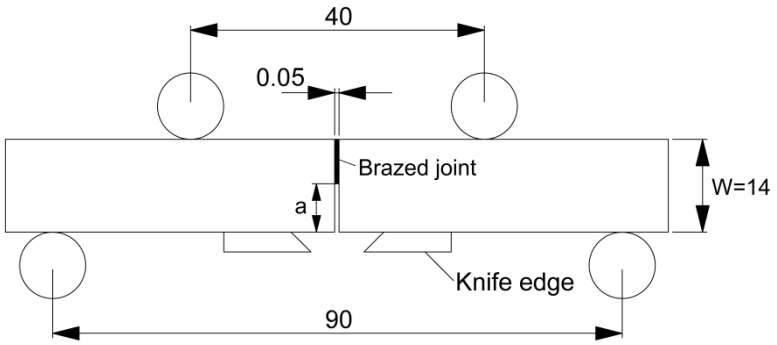

Fig.1. Schematic of the SENB specimen with initial crack length *a* (dimensions in mm)

Figure 2

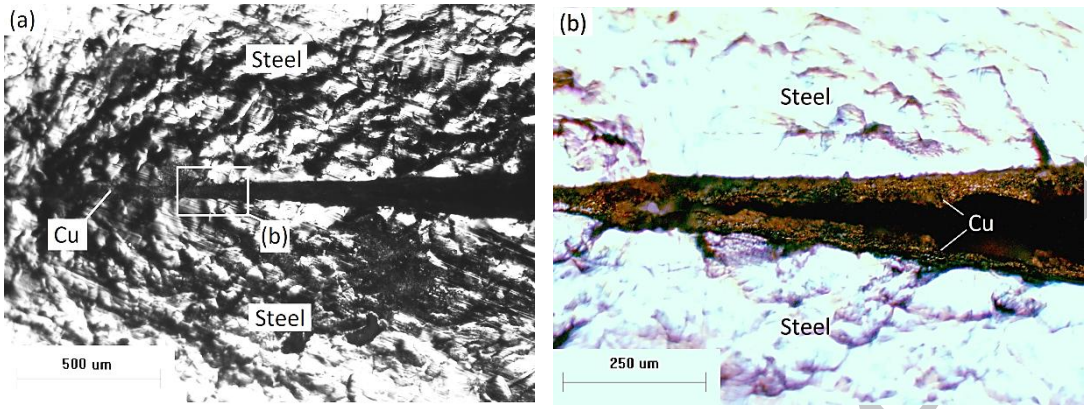

Fig.2. Optical micrograph of the SENB specimen at the crack tip region (a) 50x, (b) 100x showing the ductile tearing process within the copper filler metal and deformation in the base metal

Figure 3

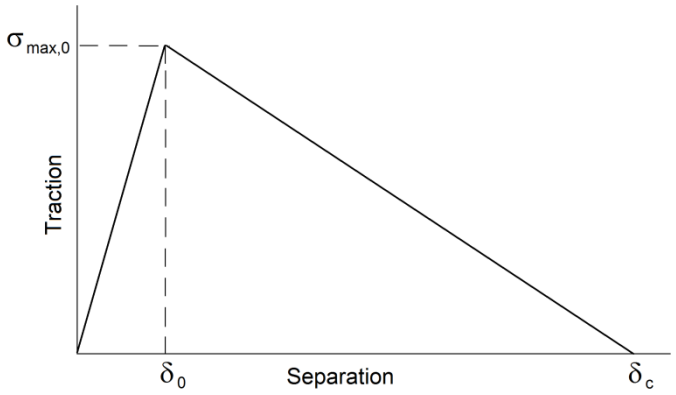

Fig.3. Bilinear traction-separation law used in the FE simulation

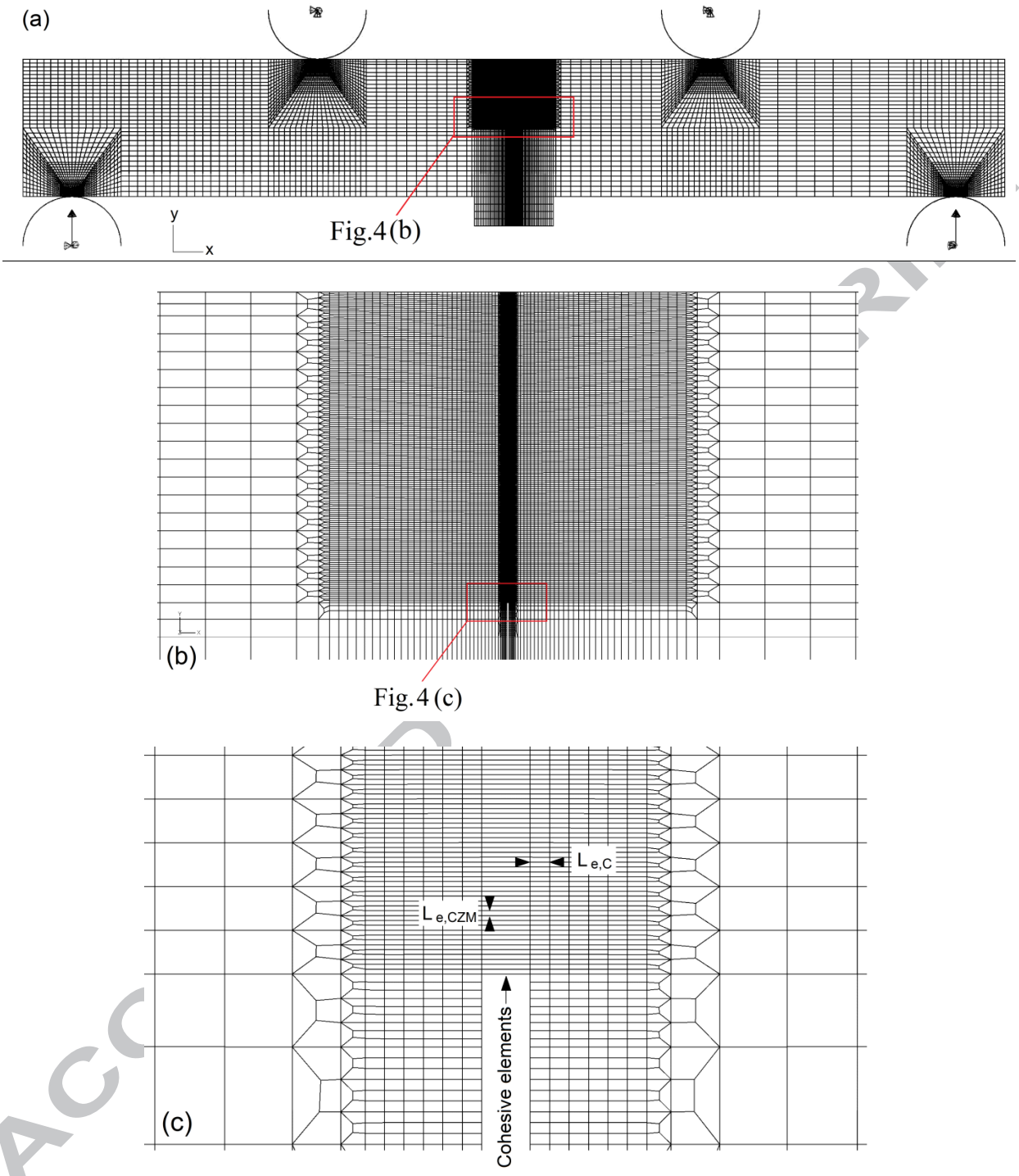

Fig.4. (a) FE model of the SENB specimens and boundary conditions, (b) mesh pattern around the crack path, (c) mesh pattern at the crack tip

Figure 5

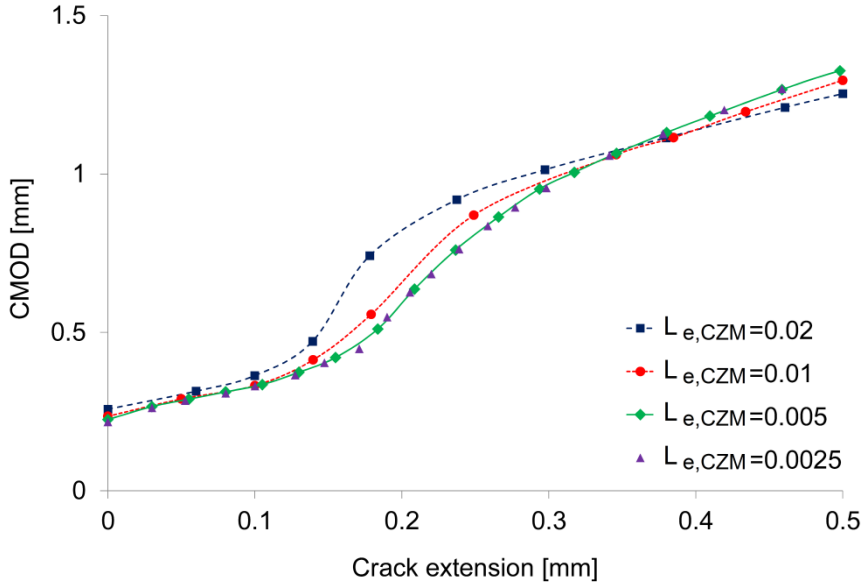

Fig.5. CMOD-crack extension curves for different cohesive element mesh sizes $L_{e,CZM}$ measured in mm

Figure 6

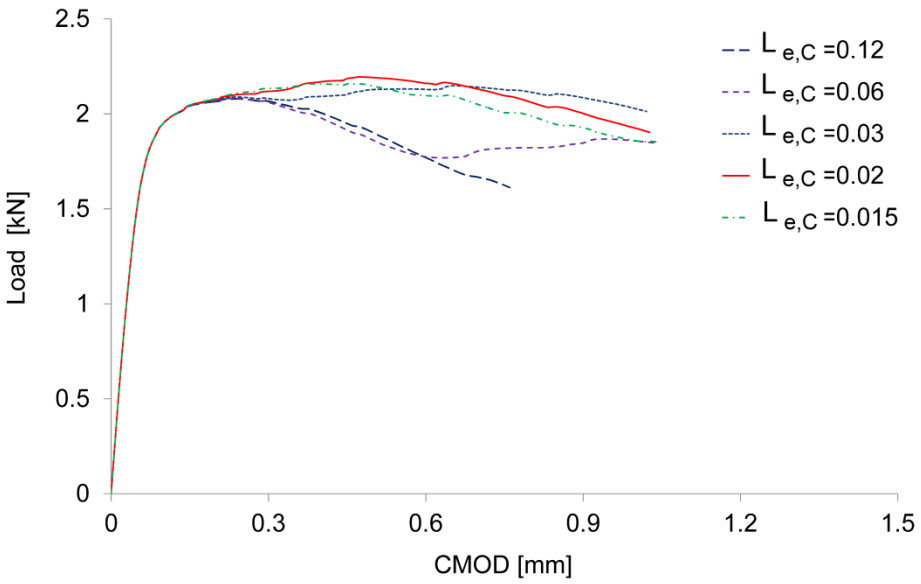

Fig.6. Load-CMOD curves for different continuum element mesh sizes $L_{e,c}$ measured in mm

Figure 7

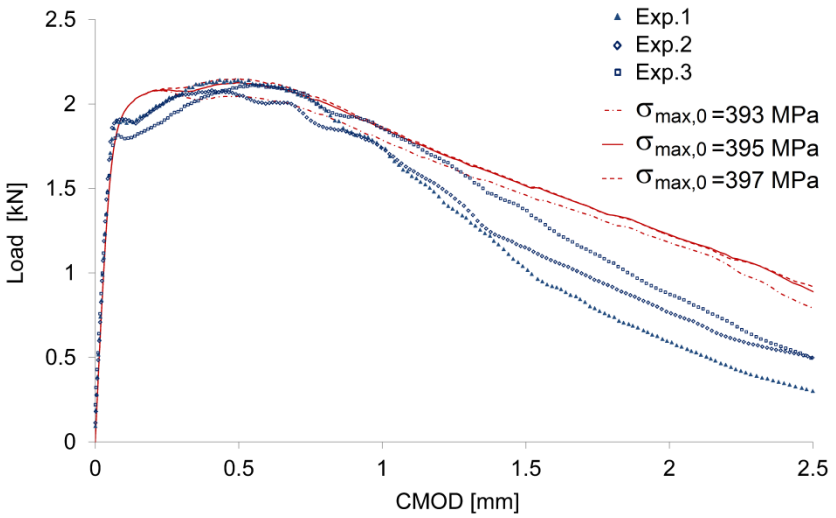

Fig.7. Numerical load-CMOD curves with different values of $\sigma_{max,0}$ fitted to the experimental results

Figure 8

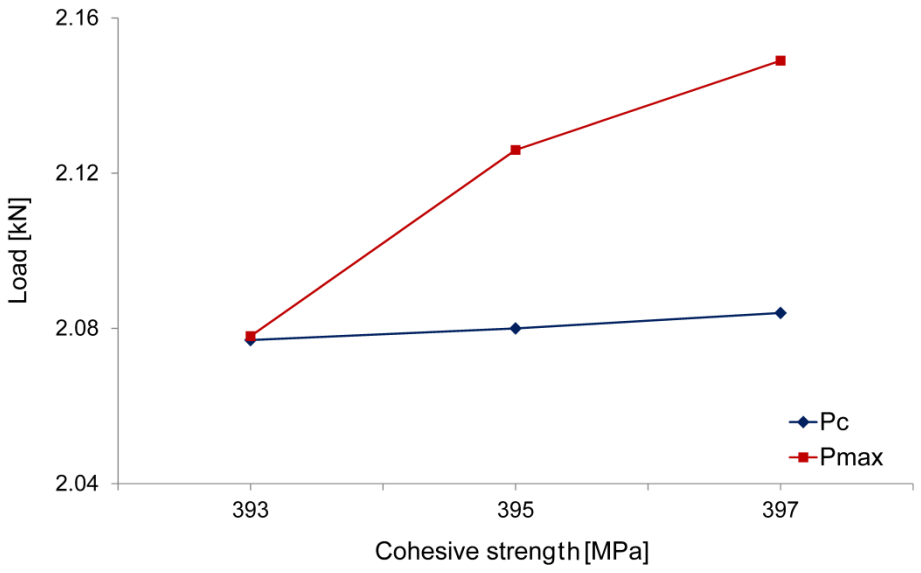

Fig. 8. Variations of the critical and maximum loads with respect to the cohesive strength

Figure 9

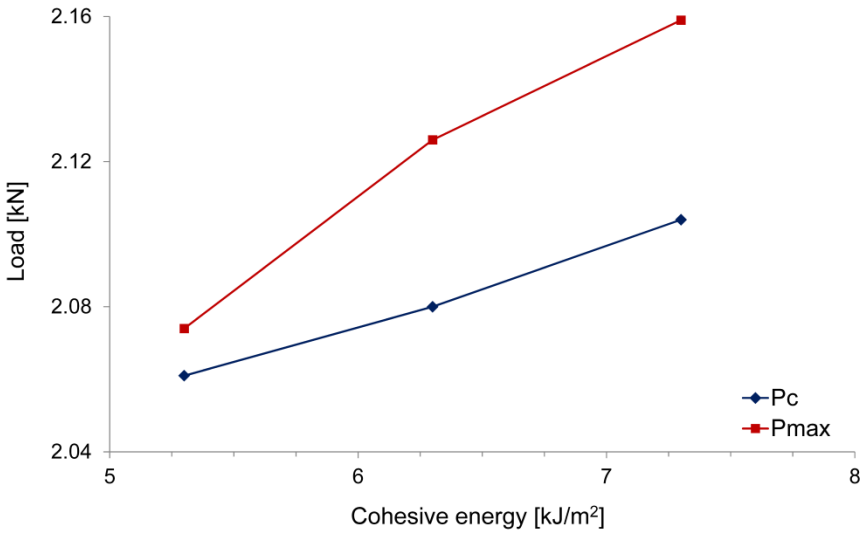

Fig.9. Variations of the critical and maximum loads with respect to the cohesive energy

Figure 10

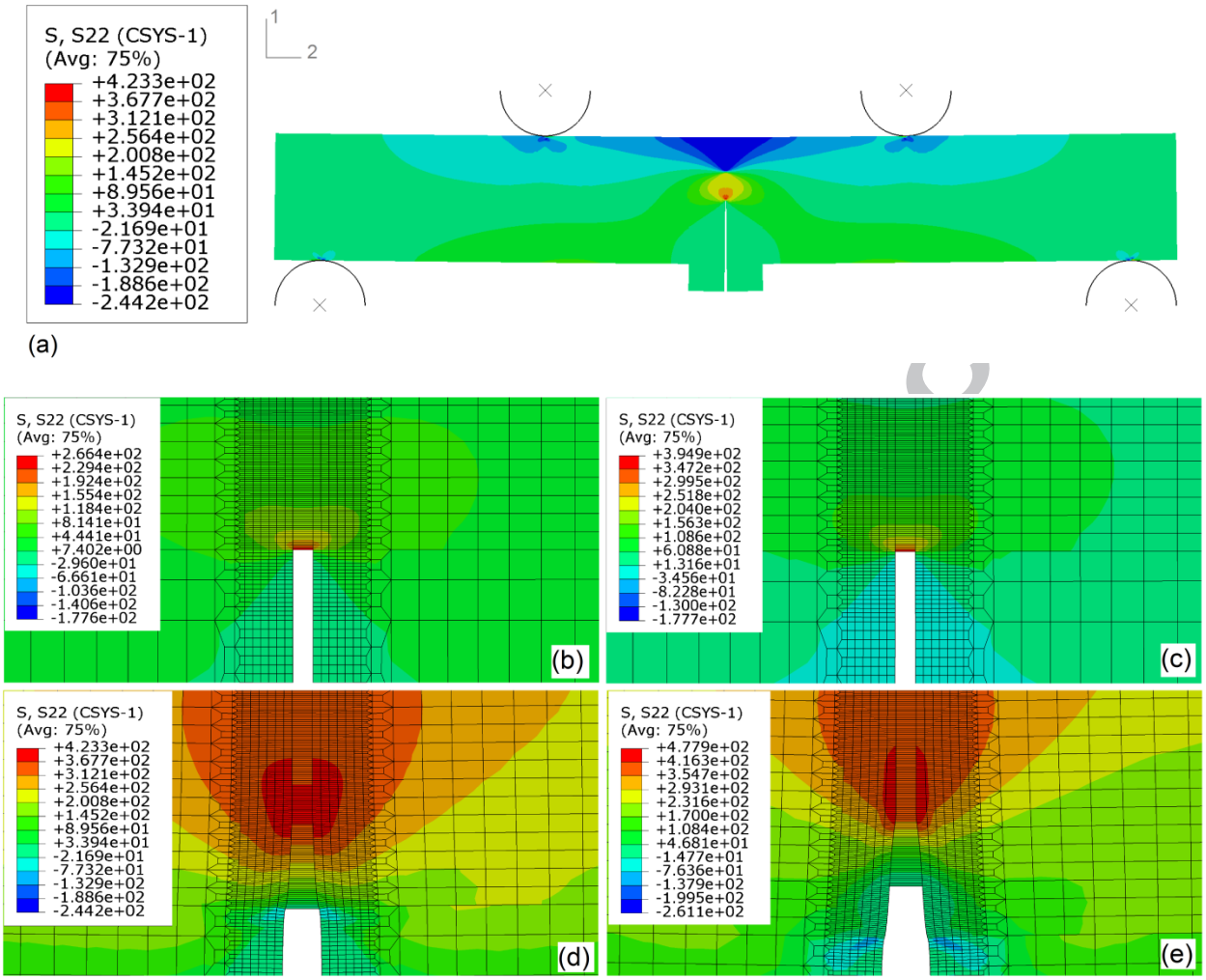

Fig.10. Stress, S22, perpendicular to crack faces (a) in the whole model at crack initiation, (b) before damage initiation, (c) at the onset of damage initiation, (d) at the onset of crack initiation, (e) during crack propagation

Figure 11

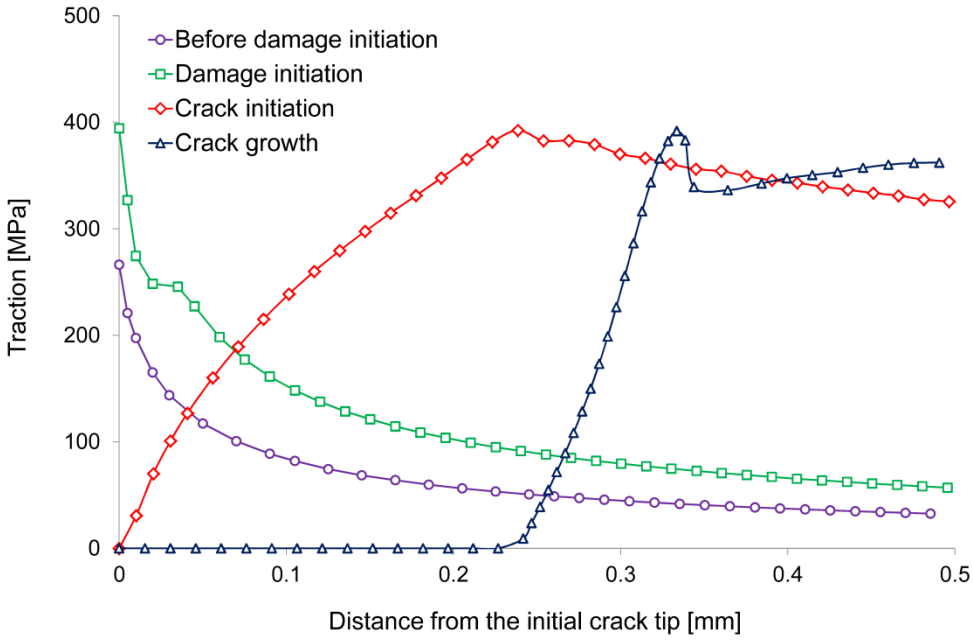

Fig.11. Traction distributions from the initial crack tip along interlayer at different damage levels

Figure 12

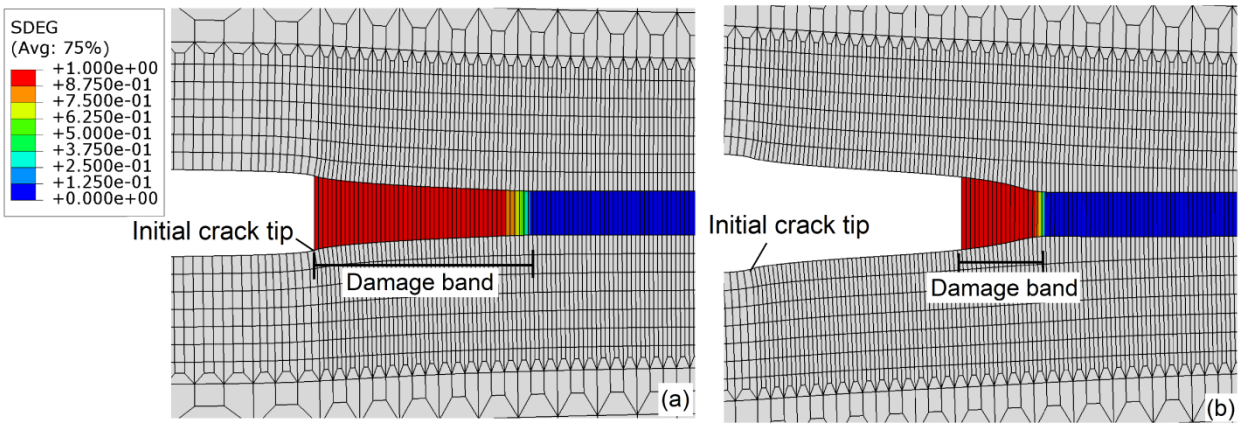

Fig. 12. Distribution of the damage variable (SDEG) along the interface (a) at the onset of crack initiation, (b) after one step crack extension ($\Delta a = 0.25\ mm$)

Figure 13

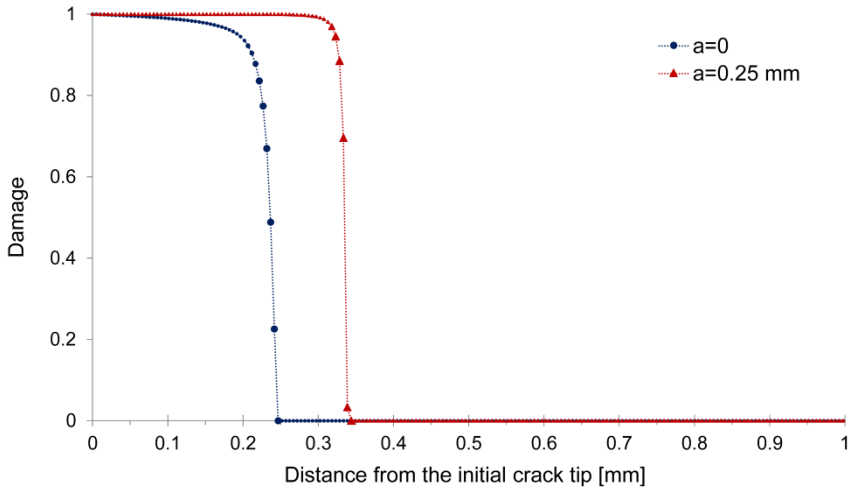

Fig. 13. Damage distribution from the initial crack tip along the interface

Figure 14

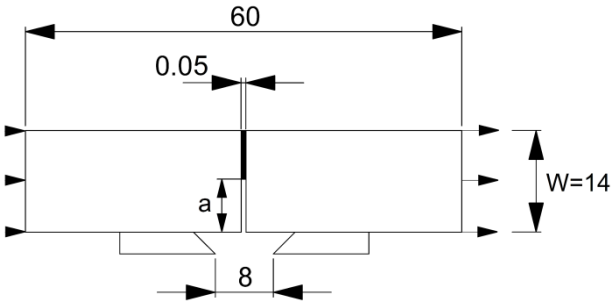

Fig.14. SENT specimen under tensile loading (dimensions in mm) [2]

Figure 15

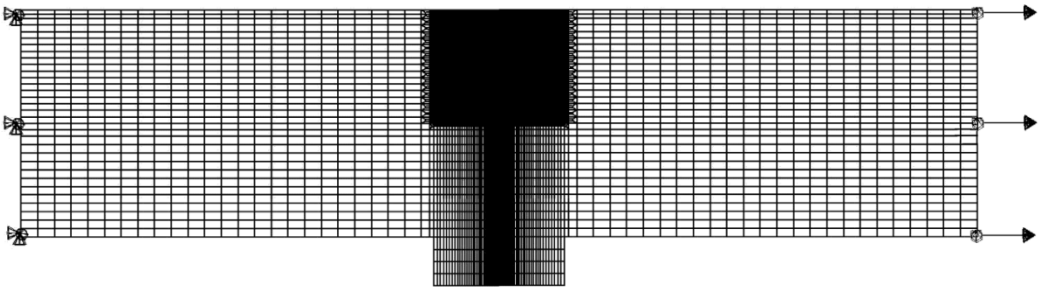

Fig.15. FE model of the SENT specimen and the applied boundary conditions

Figure 16

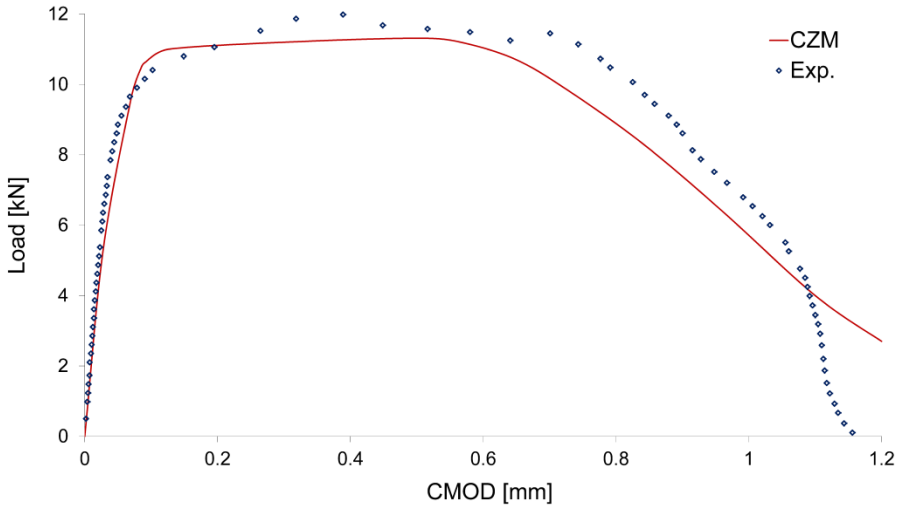

Fig.16. Experimental and numerical load-CMOD curves of the SENT specimen

Figure 17

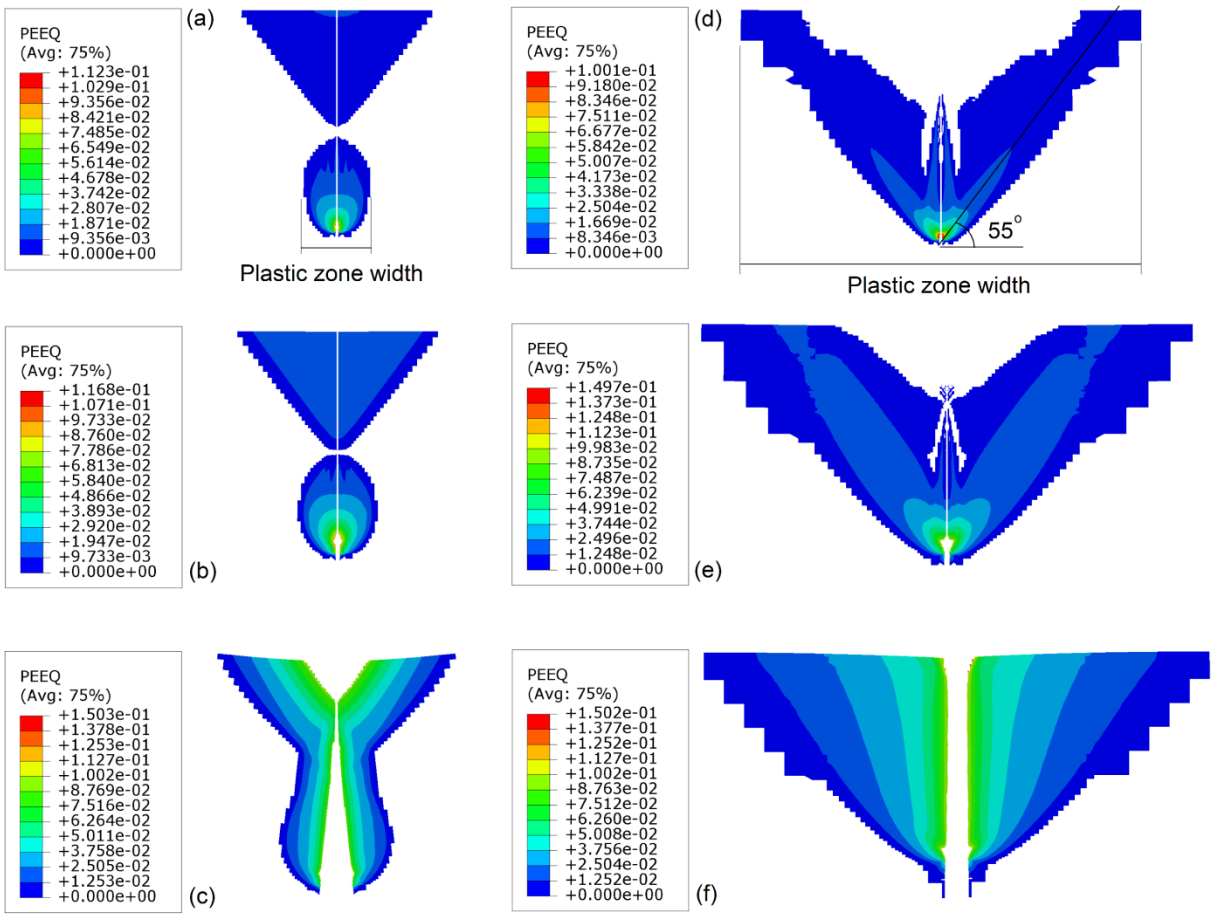

Fig.17. Contours of crack tip plastic strain in the SENB specimen (a) at crack initiation, (b) during crack propagation, (c) at the onset of failure, and in the SENT specimen (d) at crack initiation, (e) during crack propagation, (f) at the onset of failure

Figure 18

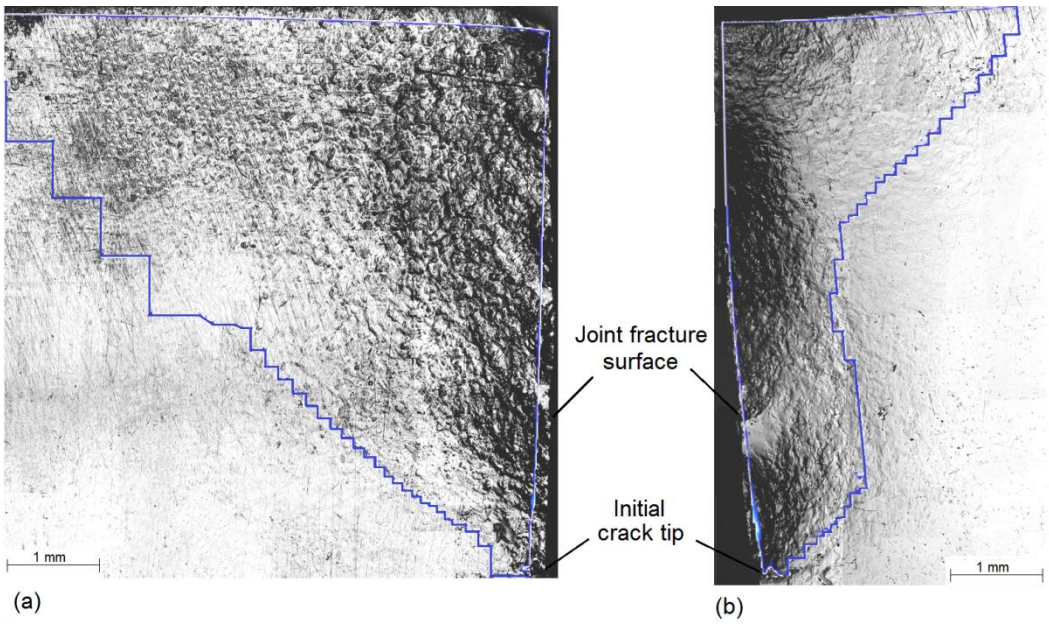

Fig.18. FE estimated plastic zones (blue lines) at the onset of failure superposed on the optical micrographs of the adjacent crack path regions of the (a) SENT and (b) SENB specimens

Figure 19

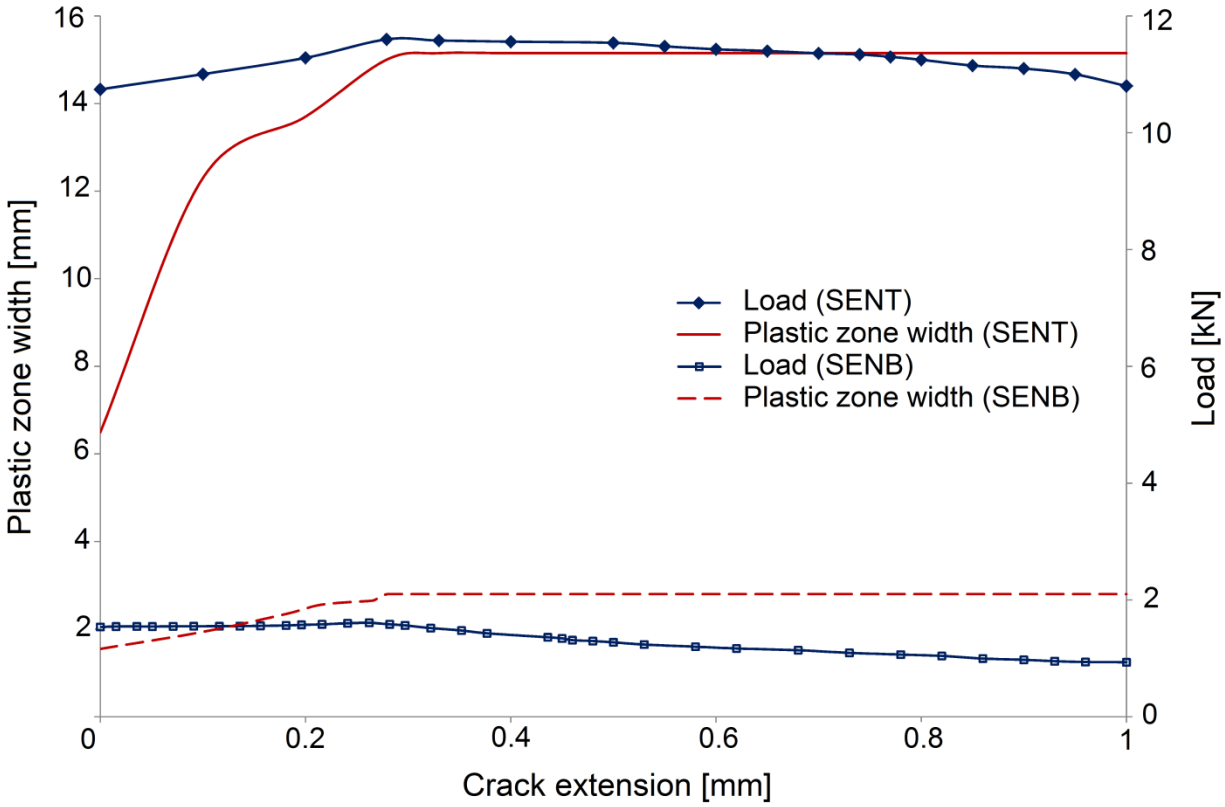

Fig.19. Load and crack tip plastic zone width with respect to the crack extension

Figure 20

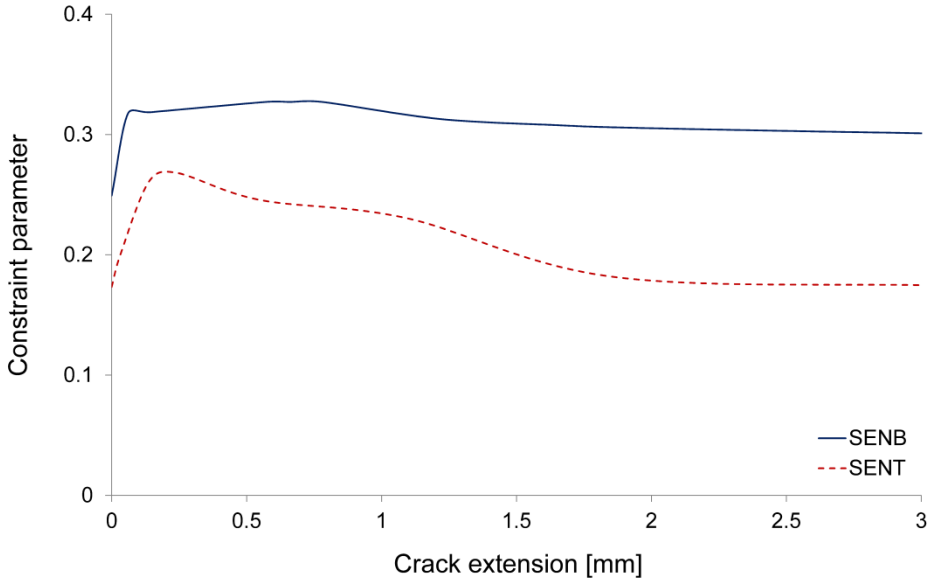

Fig.20. Crack tip constraint parameter with respect to crack extension for the SENB and SENT specimens

Nomenclature

a	Crack length
A_{Vpl}	Plastic component of the area under load-CMOD curve
b	Ligament length
B	Fracture specimen thickness
D	Damage variable
E	Young's modulus
h	Constraint parameter
J_c	Critical energy release rate
J_{el}	Elastic component of the energy release rate
J_C^{el}	Elastic component of the critical energy release rate
J_{pl}	Plastic component of the energy release rate
J_C^{pl}	Plastic component of the critical energy release rate
k	Cohesive zone stiffness
K	Stress intensity factor
$L_{e,C}$	Continuum element length
$L_{e,CZM}$	Cohesive element length
P	Load
P_c	Critical load
P_{max}	Maximum load
S_{inner}	Inner loading span
S_{outer}	Outer loading span

t	Brazed joint clearance
W	Fracture specimen width
δ	Separation
δ_0	Separation at onset of damage initiation
δ_C	Separation at failure
Γ	Cohesive energy
σ_H	Hydrostatic part of stress
$\sigma_{max,0}$	Cohesive strength
σ_{Mises}	Equivalent Mises stress

Research Highlights:

- A methodology for fracture analysis of brazed joints using the CZM is developed.
- Elastic part of the critical energy release rate is cohesive energy of brazed joints.
- The CZM predicts brazed joint fracture independent of specimen configuration.
- Effect of stress constraint on crack tip plastic zone is captured by the CZM.